Chaotic dynamics in terahertz-driven semiconductors with negative effective mass

J. C. Cao*
State Key Laboratory of Functional Materials for Informatics, Shanghai Institute of Metallurgy, Chinese Academy of Sciences, 865 Changning Road, Shanghai, 200050, People's Republic of China and Institute for Microstructural Sciences, National Research Council, Ottawa, Ontario, Canada K1A 0R6

H. C. Liu
Institute for Microstructural Sciences, National Research Council, Ottawa, Ontario, Canada K1A 0R6

X. L. Lei
Department of Applied Physics, Shanghai Jiaotong University, 1954 Huashan Road, Shanghai, 200030, People's Republic of China and State Key Laboratory of Functional Materials for Informatics, Shanghai Institute of Metallurgy, Chinese Academy of Sciences, 865 Changning Road, Shanghai 200050, People's Republic of China

A. G. U. Perera
Department of Physics and Astronomy, Georgia State University, Atlanta, Georgia 30303
(Received 11 May 2000; revised manuscript received 22 September 2000; published 26 February 2001)

We report on a detailed theoretical study of current self-oscillations and chaotic dynamics in negative effective mass (NEM) p^+pp^+ diodes driven by dc and ac electric fields with a terahertz (THz) frequency. An ''*N*-shaped'' velocity-field relation is yielded by using the nonparabolic balance-equation theory with a realistic treatment of carrier scatterings by impurity, acoustic phonon, and optic phonon. The dependence of the self-oscillating mode and its frequency on the dc bias, doping concentration, and lattice temperature is examined in detail. The THz-driven p^+pp^+ NEM diodes can produce a cooperative nonlinear oscillatory mode which leads to very complicated chaotic dynamics with the dc bias, ac amplitude, and ac frequency as the controlling parameters. The transitions between the periodic and chaotic states are carefully studied by different chaos-detecting methods, such as phase portrait, Poincaré bifurcation diagram, power spectrum, and first return map. The resulting power spectrum bifurcation diagram displays a very complicated mosaic structure with a self-similar emergence of high-order mixing frequencies.

DOI: 10.1103/PhysRevB.63.115308 PACS number(s): 73.61.Ey, 73.50.Fq, 85.30.Fg, 85.30.De

I. INTRODUCTION

Nonlinear dynamics in different kinds of semiconductor systems with dc and ac driving voltage has been a recent focus of many experimental[1–9] and theoretical[10–21] investigations. When a miniband superlattice[13,14,19,20] or a sequential resonant tunneling superlattice[4,5,10–12] is driven by dc and ac fields with GHz to THz frequency the systems can produce an alternative mode of operation and lead to the transition between the periodic state and various types of deterministic spatiotemporal chaos. Recently, by involving novel electromagnetic radiation sources and coupling techniques the effect of THz radiation field on the nonlinear current-voltage characteristics of superlattices has been investigated experimentally,[22] including multiphoton-assisted resonant tunneling,[1] negative absolute resistance,[2] and Shapiro steps on dc current-voltage curve.[3] Meanwhile, the nonlinear dynamics of a two-dimensional electron system subjected to an intense THz electric field is studied in some detail.[8,9,17] Asmar *et al.*[8,9] carried out a series of transport and optical measurements in *n*-type GaAs/AlGaAs heterojunctions and quantum wells (QW) under an intense THz irradiation. They found that the dc conductivity of these two-dimensional systems is strongly affected by the intense THz irradiation, and its behavior is sensitively dependent on the frequency and the amplitude of the radiation. Lei *et al.*[17] performed theoretical calculations of dc conductivity of *n*-QW's when the THz field is intense enough to suppress the formation of high-field domain. Basically, the above-mentioned phenomena in superlattices and QW's are related to the negative differential velocity (NDV) characteristics, which makes these systems display self-oscillating behavior. Self-oscillating systems that are forced by an external oscillating signal represent an important class of nonlinear dynamical systems.

Recently, by abstracting a NEM dispersion relation from a *p*-QW subband,[23,24] several model calculations of carrier ballistic transport in p^+pp^+ diodes have been performed, by using the collisionless Boltzmann equation[25–30] and the balance-equation theory.[21] Calculations[21] indicated that the steady-state velocity-field curve of carriers with a NEM dispersion supports an ''*N*-shaped'' section, which is quite different from the two-valley result of electron transport in bulk GaAs. Under a certain range of doping concentrations and bias fields, undamped current self-oscillation related to the formation of electric-field domain appears in the NEM p^+pp^+ diode. The oscillating frequency lies in the THz range for the NEM p^+pp^+ diodes having submicrometer *p*-base lengths. The *p*-base NEM dispersion is the origin of current oscillations in the present NEM p^+pp^+ diodes. In contrast, the current oscillation in miniband superlattice is due to the negative effective mass of Bloch electrons in the miniband. It is well known that, when electrons within the

miniband are accelerated beyond the Brillouin zone boundary, their velocity becomes negative. In the absence of scattering, the electron wave packet then oscillates with the Bloch frequency. The chaotic dynamics in superlattices driven by periodic signals have been investigated in great detail.[4,5,10–14,19,20] However, the study of chaotic dynamics in the present NEM p^+pp^+ diode is still lacking so far.

This article presents a careful study of nonlinear dynamics of the NEM p^+pp^+ diode driven by a THz signal and a dc bias at which the diode exhibits self-sustaining current oscillation. The velocity-field relation of the NEM semiconductor is calculated by the balance-equation theory, which accurately includes different scattering contributions by impurity, acoustic phonon, and optic phonon. The resulting ''*N*-shaped'' velocity-field relation (or carrier mobility) is then fed into the transient drift-diffusion (DD) model to study spatiotemporal characteristics of the NEM p^+pp^+ diodes. We have carefully calculated the dependence of self-oscillating behaviors on the applied voltage, doping concentration, and lattice temperature, and studied chaotic dynamics in the NEM p^+pp^+ diodes with the dc bias, ac amplitude, and ac frequency as the controlling parameters. The transitions between the periodic and chaotic states are extensively investigated by different chaos-detecting methods, such as phase portrait, Poincaré bifurcation diagram, power spectrum, and first return map. The power spectrum bifurcation diagram has a very complicated mosaic scenario with a self-similar emergence of high-order mixing frequencies, when the NEM p^+pp^+ diode is driven by a dc and an ac voltage with a frequency of the inverse golden mean ratio times the self-oscillating frequency.[31]

The remainder of this article is organized as follows. In Sec. II, we describe the nonparabolic balance equations for carrier transport in semiconductors and calculate the steady-state velocity-field relation of carriers with a NEM at different lattice temperatures. In Sec. III we calculate the dependence of self-oscillating current and its frequency on the applied voltage, doping concentration, and lattice temperature in NEM p^+pp^+ diodes. In Sec. IV, the spatiotemporal modes and chaotic dynamics of the diodes subject to both dc and ac voltages are extensively studied by different methods for detecting chaotic characteristics of a time series. Finally, in Sec. V we draw the main conclusions of this work.

II. ''*N*-SHAPED'' VELOCITY-FIELD RELATION OF CARRIERS WITH NEM

As shown in the previous model calculations,[25–29,21] we focus our attention on the NEM section of semiconductor dispersion by using the approximate wave-vector energy relation as follows:

$$\varepsilon(\mathbf{k})=\frac{1}{2}[\varepsilon_1(\mathbf{k})+\varepsilon_2(\mathbf{k})-\sqrt{(\varepsilon_1(\mathbf{k})-\varepsilon_2(\mathbf{k}))^2+4\Delta^2}+C]$$
$$=\frac{1}{2}\left[\frac{\hbar^2\mathbf{k}^2}{2m_e}-\sqrt{\left(\frac{\hbar^2\mathbf{k}^2}{2M_e}-\varepsilon_0\right)^2+4\Delta^2}+\sqrt{\varepsilon_0^2+4\Delta^2}\right], \quad (1)$$

in which $\mathbf{k}=(k_x,k_y,k_z)$ is a three-dimensional wave vector, $\varepsilon_1(\mathbf{k})=\hbar^2\mathbf{k}^2/(2m)$, $\varepsilon_2(\mathbf{k})=\hbar^2\mathbf{k}^2/(2M)+\varepsilon_0$, m and M are two effective masses, and Δ and ε_0 are two energy-band-related energies. We denote $C\equiv\sqrt{\varepsilon_0^2+4\Delta^2}-\varepsilon_0$, $m_e\equiv Mm/(M+m)$, and $M_e\equiv Mm/(M-m)$. When $M\to m$, the dispersion (1) reduces to a parabolic band. According to the balance-equation theory, when a uniform electric field $\mathbf{E}$ is applied to the semiconductor with an energy–wave-vector relation $\varepsilon(\mathbf{k})$, the transport state of the carriers can be described by the average center-of-mass momentum $\mathbf{p}_d$ and the relative carrier temperature T_c, which are determined by the steady-state effective acceleration- and energy-balance equations,[31,32]

$$0=en\mathbf{E}\cdot\mathcal{K}+\mathbf{A}_{\rm ei}+\mathbf{A}_{\rm ep}, \quad (2)$$

$$0=en\mathbf{E}\cdot\mathbf{v}_d-W_{\rm ep}. \quad (3)$$

In Eqs. (2) and (3), e is the carrier charge, and

$$n=\frac{1}{4\pi^3}\int d^3k f((\varepsilon(\mathbf{k})-\mu)/k_{\rm B}T_c) \quad (4)$$

is the carrier density, $\mathbf{v}_d=\langle\nabla\varepsilon(\mathbf{k})\rangle$ is the average velocity, $\varepsilon=\langle\varepsilon(\mathbf{k})\rangle$ is the average energy, and $\mathcal{K}=\langle\nabla\nabla\varepsilon(\mathbf{k})\rangle$ is the ensemble-averaged inverse-effective-mass tensor of the carriers. Here $\langle\cdots\rangle$ stands for the weighted integral over a Brillouin zone in $\mathbf{k}$ space: $\langle\cdots\rangle=1/(4\pi^3n)\int d^3k f([\varepsilon(\mathbf{k}-\mathbf{p}_d)-\mu]/k_{\rm B}T_c)\cdots$, with $f(x)=1/[\exp(x)+1]$ the Fermi distribution function and μ the chemical potential. The frictional acceleration $\mathbf{A}_{\rm ei}$, $\mathbf{A}_{\rm ep}$ (due to impurity and phonon scatterings) and the energy-loss rate $W_{\rm ep}$ (due to phonon scattering) share the same expressions as those given in Refs. 32 and 33. They are completely determined by $\mathbf{p}_d$, T_c, and μ (or n) for a semiconductor system with known impurity distributions, phonon modes, electron-impurity potentials, and electron-phonon coupling matrix elements. The explicit expressions of acceleration and energy-loss rate can be found in Ref. 21.

From Eqs. (2) and (3) we have calculated the steady-state carrier drift velocities as a function of the electric field E. Hole-impurity, hole-acoustic-phonon (deformation and piezoelectric), hole-polar-optic-phonon, and hole-nonpolar-optic-phonon are taken into account in the calculations. Parameters appearing in the dispersion (1) are $m=0.085m_0$ (m_0 is the free electron mass), $M=0.54m_0$, $\varepsilon_0=0.1$ eV, and $\Delta=0.02$ eV. They are the same as those used in Refs. 26 and 21. The dispersion diagram calculated from Eq. (1) is shown in Fig. 1(a). The device structure considered here is a p^+pp^+ diode, which is shown in the inset of Fig. 1(a). All other material constants used in calculations are typical values of bulk GaAs: lattice density 5.31 g/cm^3, transverse sound velocity $v_{st}=2.48\times10^3$ m/s, longitudinal sound velocity $v_{sl}=5.29\times10^3$ m/s, LO phonon energy $\Omega_{\rm LO}=35.4$ meV, low-frequency dielectric constant $\kappa=12.9$, optical dielectric constant $\kappa_\infty=10.8$, valence-band deformation potential $\Xi=8.5$ eV, and piezoelectric constant $e_{14}=1.41\times10^9$ V/m. From these given material parameters and given carrier density, $A_{\rm ei}$, $A_{\rm ep}$, and $W_{\rm ep}$ are completely determined as functions of p_d and T_c. They are in forms of multilayer integrations and have been numerically calculated by the ten-point Gauss integration method.

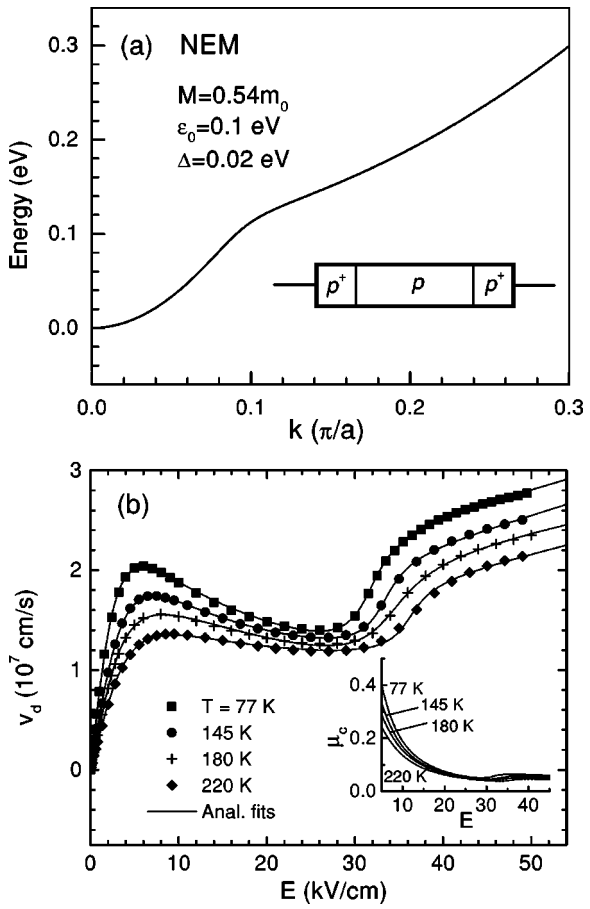

FIG. 1. (a) A model dispersion calculated from Eq. (1). The parameters are $m=0.085m_0$ (m_0 is the free electron mass), $M=0.54m_0$, $\varepsilon_0=0.1$ eV, and $\Delta=0.02$ eV. a is the lattice constant. The inset is the p^+pp^+ device structure considered here. (b) Calculated carrier drift velocity v_d (symbols) as a function of the steady-state electric field E at carrier density $n=1.0\times10^{17}$ cm^{-3} and different lattice temperatures $T=77$, 145, 180, and 220 K, respectively. The lines are the analytical fits by Eq. (5). The inset is the field-dependent carrier mobility in unit of m^2 /Vs.

The calculated carrier drift velocity v_d is shown in Fig. 1(b) as a function of the steady-state electric field E at carrier density $n=1.0\times10^{17}$ cm^{-3} for different lattice temperatures $T=77$, 145, 180, and 220 K. All velocity-field curves have an ''N-shaped'' NDV. The NDV becomes less pronounced when lattice temperature is increased. When $T=77$ K the peak velocity is about 2×10^7 cm/s at the critical electric field $E_c=6$ kV/cm. When $T=220$ K the peak velocity decreases to about 1.36×10^7 cm/s at the critical electric field $E_c=9$ kV/cm. Near $E=27$ kV/cm, in all velocity-field relations the differential velocity becomes positive. This kind of ''N-shaped'' NDV is somewhat similar to that of a sequential resonant tunneling superlattice,[11] but is different from that for electrons in two-valley bulk GaAs. We have found an analytical formula to fit the velocity-field relation as follows:

$$v_d=C_1E\left[1-C_2\frac{E^2+C_3}{E^2+C_4E+C_5}+C_6\arctan(C_7E-C_8)\right], \tag{5}$$

TABLE I. The values of C_i ($i=1,2,\ldots,8$) appearing in Eq. (5) at lattice temperatures $T=77$, 145, 180, and 220 K, respectively.

T	77 K	145 K	180 K	220 K
C_1	1.31350	1.21857	1.28112	0.84975
C_2	0.99616	0.98858	1.00000	0.98499
C_3	5.85828	15.23651	13.27141	18.43012
C_4	1.00716	0.69681	1.09615	0.97544
C_5	15.30504	27.16247	19.82886	31.08370
C_6	0.01087	0.00858	0.00984	0.00869
C_7	0.40437	0.44017	0.25371	0.45676
C_8	12.78973	14.63324	8.65393	16.50578

in which v_d is in units of 10^7 cm/s and E is in kV/cm. The values of C_i ($i=1,2,\ldots,8$) for $T=77$, 145, 180, and 220 K are listed in Table I. In the whole range of electric fields considered here, a good agreement is observed from Fig. 1(b) between the analytical results (solid lines) by Eq. (5) and the balance-equation calculations (solid symbols).

III. SELF-SUSTAINING OSCILLATIONS UNDER dc BIAS

In this section, we carry out calculations of current oscillations in p^+pp^+ diodes [see the inset of Fig. 1(a)] with a NEM p-base under a dc bias by using the transient drift-diffusion equations and the Poisson equation. The mobility of carriers in p base is given by Eq. (5),

$$\mu_c=v_d/E=C_1[1-C_2(E^2+C_3)/(E^2+C_4E+C_5)+C_6\arctan(C_7E-C_8)],$$

which is shown in the inset of Fig. 1(b). The numerical scheme to solve these equations has been described in some detail in Ref. 21. Electrostatic potential $\phi(x,t)$ and hole density $n(x,t)$ are the time- and space-dependent fundamental unknown variables that we need to solve. All other quantities, such as electric field $E(x,t)=-\partial\phi/\partial x$, hole velocity v_d, and conduction hole current density $j(x,t)=env_d$, can be obtained from the fundamental variables. The total current density is the sum of the conduction current density and the displacement current density,

$$J(t)=j(x,t)+\kappa\epsilon_0\frac{\partial E(x,t)}{\partial t}, \tag{6}$$

which is a function of time t only. In Eq. (6), κ is the dielectric constant of the p-base material. For the p^+pp^+ structure subjected to dc and ac voltages in the form

$$V(t)=V_{\rm dc}+V_{\rm ac}\sin(2\pi f_{\rm ac}t), \tag{7}$$

the boundary conditions for $\phi(x,t)$ and $n(x,t)$ are as follows:

$$\phi(x_L,t)=0, \quad \phi(x_R,t)=V(t), \tag{8}$$

$$n(x_L,t)=N_a(x_L), \quad n(x_R,t)=N_a(x_R), \tag{9}$$

in which $V_{\rm ac}$ and $f_{\rm ac}$ are, respectively, the amplitude and frequency of ac voltage, x_L and x_R stand for the position of

the left and right p^+ contact boundaries, and $N_a(x)$ is the doping concentration. The initial values $\phi(x,0)$ and $n(x,0)$ are set to be the thermal-equilibrium values at zero bias condition.

In the calculations, the contact doping concentration is set to be $N_a(x_L)=N_a(x_R)=2\times10^{18}$ cm^{-3}. The length of p-base is defined as l, and each p^+-base length is $l/2$. For all calculations, we set p-base length $l=0.5$ μm. We exponentially smooth the doping concentration near the p^+p and pp^+ junctions for the sake of numerical stability. To mimic a realistic situation, we assume that there is a slight doping fluctuation near the cathode end of the diode, which is the origin of the formation of electric field domain. For a NDV system, any small fluctuation of internal inhomogeneity (doping or field) may give rise to the formation of a traveling high-field domain due to the spatial amplification and temporal growth, so the existence of a NDV section [see Fig. 1(b)] in the stationary velocity-field relation may cause a global current instability in realistic devices under certain conditions. We apply the standard finite-difference technique to solve the DD model. It is observed that, for the p^+pp^+ NEM diodes with a p-base length $l=0.5$ μm simulated here, 300 space meshpoints and 1.5×10^{-3} ps time step exhibit a good numerical accuracy and stability. In general, no more than five Newton iterations usually reach convergence for every time step at all applied voltages within a maximum relative error of 10^{-4} for the variables $\phi(x,t)$ and $n(x,t)$.

We now consider the pure dc case ($V_{ac}=0$). When the applied dc bias V_{dc} is larger than a critical value the self-sustaining periodic current oscillations show up with a frequency f_s. We define the time-averaged current density J_{av} by integrating $J(t)$ over one oscillating period $T_s(=1/f_s)$,

$$J_{av}=\frac{1}{T_s}\int_{t_1}^{t_1+T_s}J(t)dt, \tag{10}$$

in which t_1 is a time after the transient response dies out.

Calculations indicate that, for given V_{dc} biased in the NDV regime, the carrier concentration has a strong effect on the modes of electric field domains. Undamped time-periodic current self-oscillations show up when the doping density N_a is between two critical values N_a^* and N_a^{**}. The self-oscillating frequency depends on the doping concentrations.[21] Below N_a^* and above N_a^{**} the currents exhibit no oscillations after a few picosecond transient responses. On the other hand, for a given doping concentration N_a, there are two critical values V_{dc}^* and V_{dc}^{**}. Only when $V_{dc}^*<V_{dc}<V_{dc}^{**}$, the diode is biased in the NDV regime, the self-oscillation shows up. In Fig. 2 we show the temporal evolution of the current $J(t)$ for the p^+pp^+ diode with the doping concentration $N_a=6.6\times10^{17}$ cm^{-3} at different dc biases $V_{dc}=0.235$, 0.25, 0.27, 0.3, 0.32, 0.6, 0.98, and 1.14 V, respectively. The oscillating patterns and frequencies are obviously different with changing V_{dc}. The occurrences of current self-oscillations indicate that dynamic electric-field domains are formed. In Fig. 3, we show the dependence of time-averaged current densities J_{av} and static-state current densities J_{sta} on dc biases from $V_{dc}=0.1$ to 1.3 V at $T=77$ K

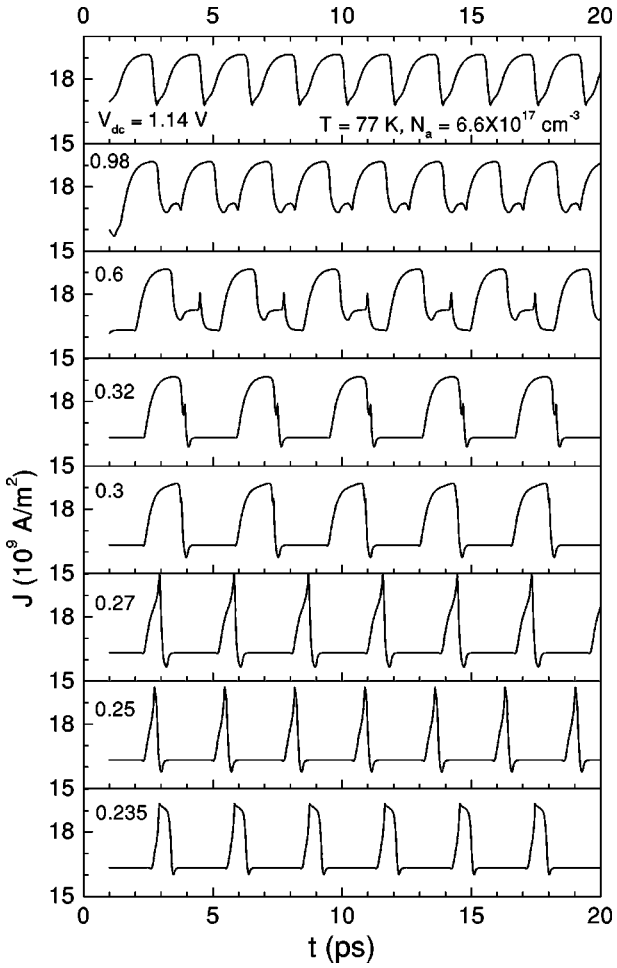

FIG. 2. Temporal evolution of the current densities $J(t)$ for the NEM p^+pp^+ diode having p-region doping concentration $N_a=6.6\times10^{17}$ cm^{-3} at different dc biases $V_{dc}=0.235$, 0.25, 0.27, 0.3, 0.32, 0.6, 0.98, and 1.14 V, respectively. In the whole article, the p-region length is set to be $l=0.5$ μm.

and different doping concentrations $N_a=0.6$, 1.0, 1.8, 3.0, 4.8, and 6.6×10^{17} cm^{-3}, respectively. All solid points correspond to the current densities when static electric-field domains are formed, i.e., after the transient dies out, the current approaches a constant. The open points stand for the time-averaged current densities J_{av} defined by Eq. (10) when dynamic electric-field domains are formed. These dynamic dc voltage bands expand with increasing doping concentration. When $N_a=0.6\times10^{17}$ cm^{-3} the dynamic dc voltage band is from 0.295 to 1.05 V, and when $N_a=6.6\times10^{17}$ cm^{-3} the dynamic dc band expands to a region from 0.235 to 1.14 V. We also note that, at larger doping concentrations, the dynamic dc voltage band is offset with the static band. When the doping concentration decreases, the dynamic band becomes continuous with the static band.

The dependence of self-oscillating frequencies f_s on dc bias is shown in Fig. 4 at $T=77$ K and for different doping concentrations $N_a=0.6$, 1.0, 1.8, 3.0, 4.8, and 6.6×10^{17} cm^{-3}. The self-oscillating frequencies are between 0.25 and 1.2 THz. For low doping concentrations $N_a=0.6$ and 1.0×10^{17} cm^{-3}, the critical voltages of transition from

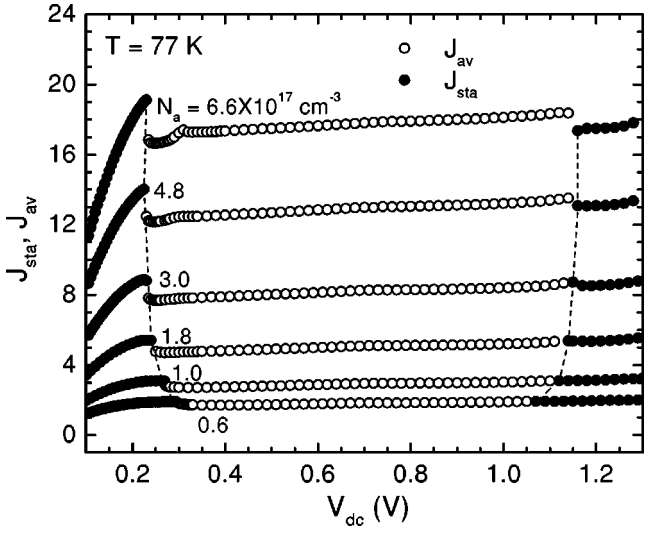

FIG. 3. Dependence of time-averaged current densities J_{av} (open circles) and static-state current densities J_{sta} (solid circles) on dc biases from 0.1 to 1.3 V at $T=77$ K and different doping concentrations $N_a=0.6$, 1.0, 1.8, 3.0, 4.8, and 6.6×10^{17} cm^{-3}, respectively.

quenched mode to transit-time mode[18] are about 0.3 and 0.271 V, respectively. In the regions of quenched modes ($V_{dc}<0.3$ V for $N_a=0.6\times10^{17}$ cm^{-3} and $V_{dc}<0.271$ V for $N_a=1.0\times10^{17}$ cm^{-3}) the self-oscillating frequencies decrease rapidly with increasing dc bias voltage, while in the regions of transit-time modes ($V_{dc}>0.3$ V for $N_a=0.6\times10^{17}$ cm^{-3} and $V_{dc}>0.271$ V for $N_a=1.0\times10^{17}$ cm^{-3}) the frequencies increase with increasing dc voltages. The two kinds of modes can be understood from that, when the dc bias is turned on, electric field domain is created and then it moves toward the anode. Depending on the applied bias, the electric field domain may or may not reach the anode before it disappears. The former case is transit-time mode, while the latter case corresponds to quenched mode. The period of the oscillation is mainly determined by the total traveling time of

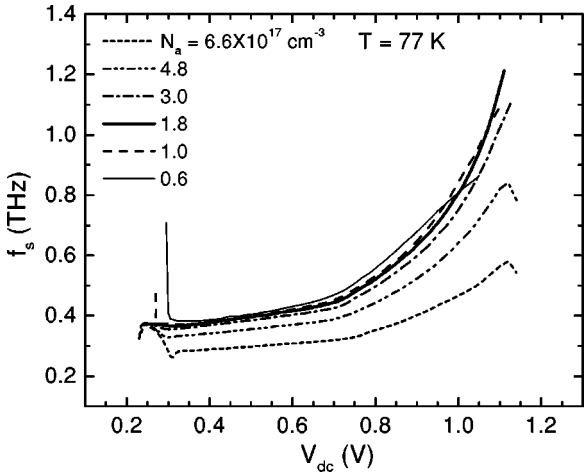

FIG. 4. Dependence of self-oscillating frequencies f_s on dc biases from 0.1 to 1.3 V at $T=77$ K and different doping concentrations $N_a=0.6$, 1.0, 1.8, 3.0, 4.8, and 6.6×10^{17} cm^{-3}, respectively.

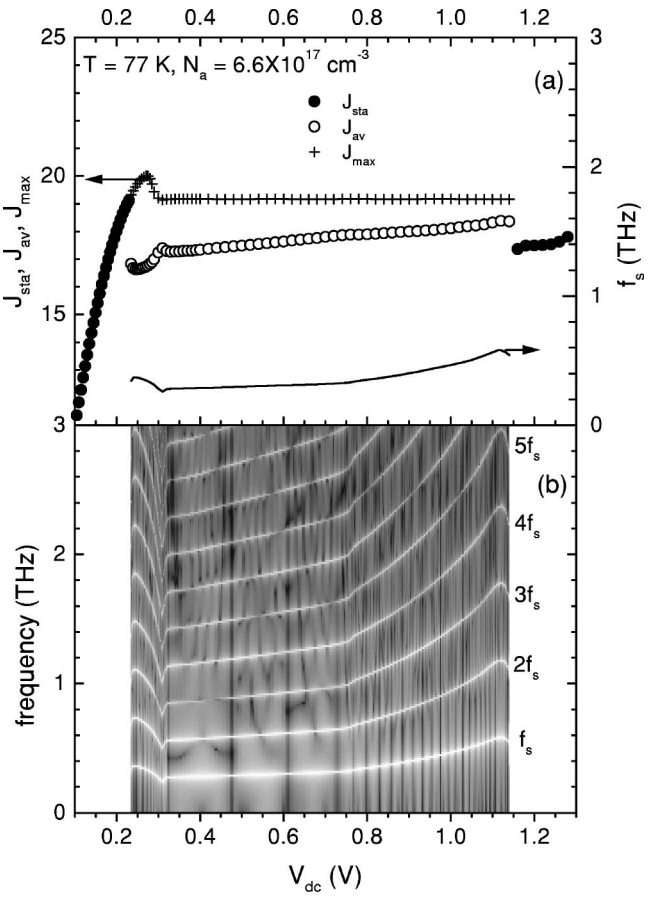

FIG. 5. (a) Dependence of self-oscillating frequency f_s, time-averaged current density J_{av}, static current density J_{sta}, and the amplitude J_{max} on dc biases from 0.1 to 1.3 V at $T=77$ K and $N_a=6.6\times10^{17}$ cm^{-3}. (b) The corresponding power spectrum bifurcation diagram, in which lighter areas correspond to larger amplitudes of PS. The lowest bright line is the self-oscillating frequency f_s, and the upper bright lines respectively correspond to its harmonics mf_s ($m=2,3,\ldots$).

the accumulation wave across the p base. The formation and traveling of electric field domains in the present p^+pp^+ NEM diode are somewhat similar to the domain modes appearing in the well-known Gunn transferred-electron devices,[34] but their microscopic mechanisms are different. In Gunn devices electrons transfer from the high-mobility lower valley to the low-mobility upper valley, leading to a NDV, while the NDV in the present p^+pp^+ diode results from a single band with a NEM section. It is worth noting that in the present ''N-shape'' velocity-field relation there is a positive-differential-velocity section after the NDV region. This property results in an increase of oscillation frequency of the NEM p^+pp^+ diode, when compared to Gunn devices.

To have a better insight into the dynamic dc band, in Fig. 5(a) we show the dependence of amplitude J_{max}, time-averaged current density J_{av}, static-state current density J_{sta}, and self-oscillating frequency f_s (right axis) on dc biases from 0.1 to 1.3 V at $T=77$ K and doping concentrations $N_a=6.6\times10^{17}$ cm^{-3}. The corresponding power spectrum (PS) bifurcation diagram is shown in Fig. 5(b) for the dynamic dc band between 0.235 and 1.14 V. The power spec-

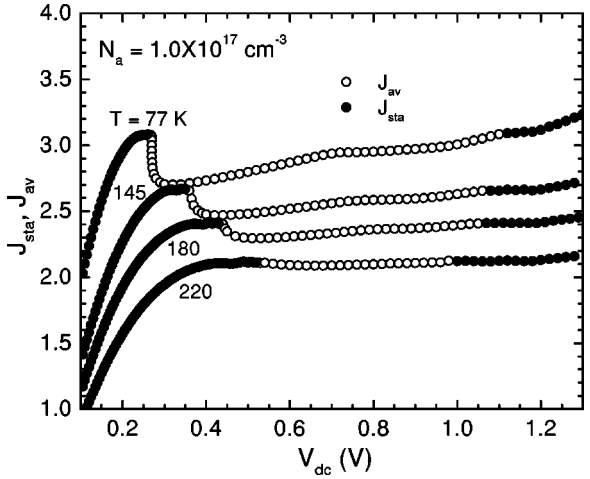

FIG. 6. Dependence of time-averaged current densities J_{av} and static-static current densities J_{sta} on dc biases from 0.1 to 1.3 V at $N_a=1.0\times10^{17}$ cm^{-3} and different lattice temperatures $T=77$, 145, 180, and 220 K, respectively.

trum (PS) is calculated by using a fast Fourier transform algorithm. The step of V_{dc} is set to be 1.5 mV. The logarithmic PS's are shown as a density plot, where lighter areas correspond to larger amplitudes of PS. The lowest bright line is the self-oscillating frequency f_s, and the upper bright lines respectively correspond to its harmonics mf_s $(m=2,3,\ldots)$.

The temperature-dependent time-averaged current-voltage characteristics are also studied and shown in Fig. 6 for a NEM p^+pp^+ diode having doping concentration $N_a=1.0\times10^{17}$ cm^{-3} at different lattice temperatures $T=77$, 145, 180, and 220 K, respectively. The time-averaged dc current J_{av} decreases with increasing lattice temperature at a given dc voltage, since the average hole velocity decreases with increasing lattice temperature as indicated in Fig. 1(b). The corresponding self-oscillating frequencies f_s on dc biases are shown in Fig. 7. All the frequencies versus the dc voltages have an obvious transition from quenched mode to transit-

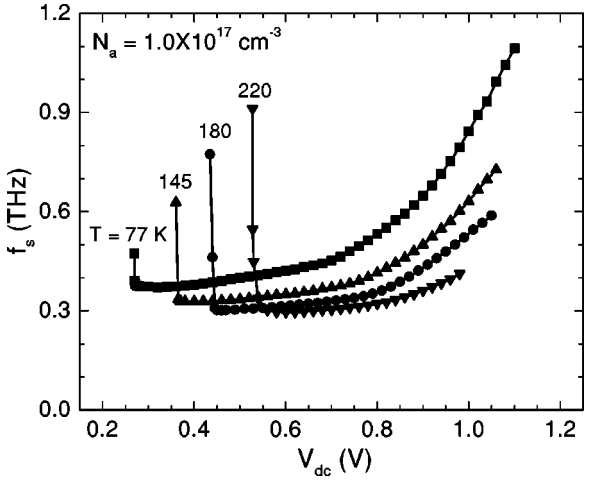

FIG. 7. Dependence of oscillating frequency f_s on dc biases from 0.1 to 1.3 V at $N_a=1.0\times10^{17}$ cm^{-3} and different lattice temperatures $T=77$, 145, 180, and 220 K, respectively.

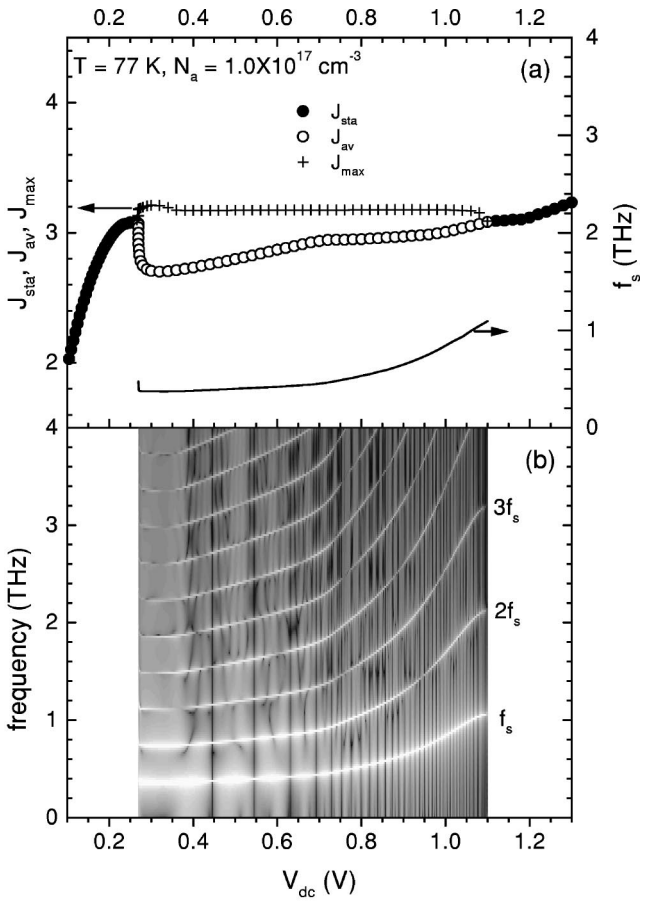

FIG. 8. (a) Dependence of self-oscillating frequency f_s, time-averaged current density J_{av}, static current density J_{sta}, and the amplitude J_{max} on dc biases from 0.1 to 1.3 V at $T=77$ K and $N_a=1.0\times10^{17}$ cm^{-3}. (b) The corresponding power spectrum bifurcation diagram.

time mode. For the case of $T=77$ K and $N_a=1.0\times10^{17}$ cm^{-3}, we show in Fig. 8(a) the dependence of amplitude J_{max}, time-averaged current densities J_{av}, static-state current densities J_{sta}, and self-oscillating frequency f_s (right axis) on dc biases from 0.1 to 1.3 V. Calculations of PS's similar to Fig. 5(b) are carried out and shown in Fig. 8(b) versus dc bias from 0.2694 to 1.1 V. The main difference between Fig. 5(a) and Fig. 8(a) is that the current densities in the latter case are almost continuous between the dynamic dc band and static dc band.

IV. TRANSITION BETWEEN PERIODIC AND CHAOTIC STATES

In this section, we deal with the NEM p^+pp^+ diode driven both by dc and ac voltages. When the NEM diode is subject to a periodic voltage expressed by Eq. (7), a variety of spatiotemporal behaviors have been found, depending on the dc bias V_{dc}, ac amplitude V_{ac}, and ac frequency f_{ac}. First, we consider the ac amplitude V_{ac} as the controlling parameter, while the dc voltage is fixed to $V_{\mathrm{dc}}=1$ V, which leads to a self-oscillating frequency $f_s=0.84$ THz for the NEM p^+pp^+ diode with a doping concentration $N_a=1.0$

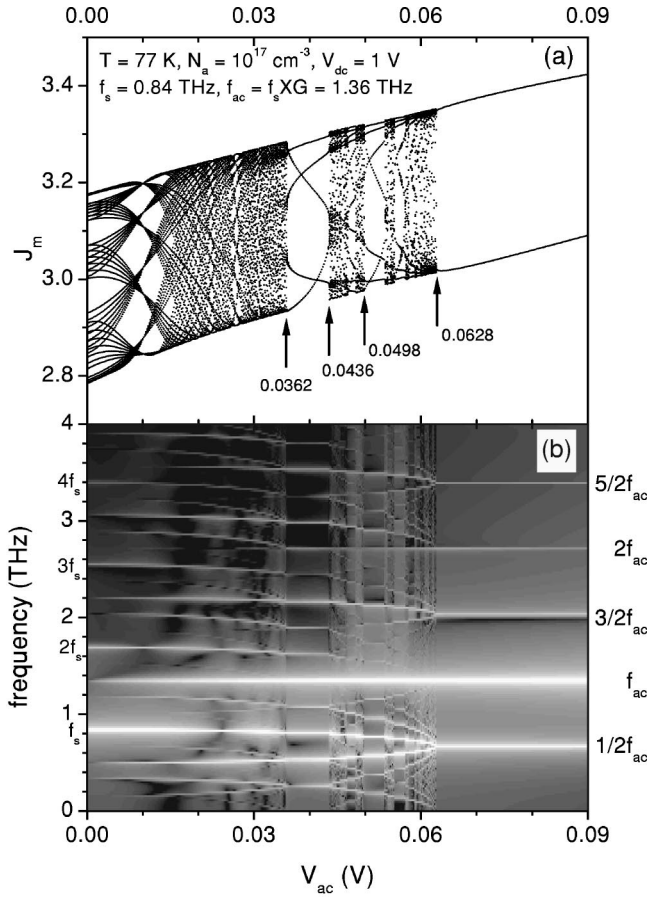

FIG. 9. (a) Poincaré bifurcation diagram and (b) power spectrum bifurcation diagram at $T=77$ K, $N_a=1.0\times10^{17}$ cm^{-3}, $V_{\rm dc}=1$ V, $f_s=0.84$ THz, and $f_{\rm ac}=f_s\times G\approx1.36$ THz with G the inverse Golden mean ratio.

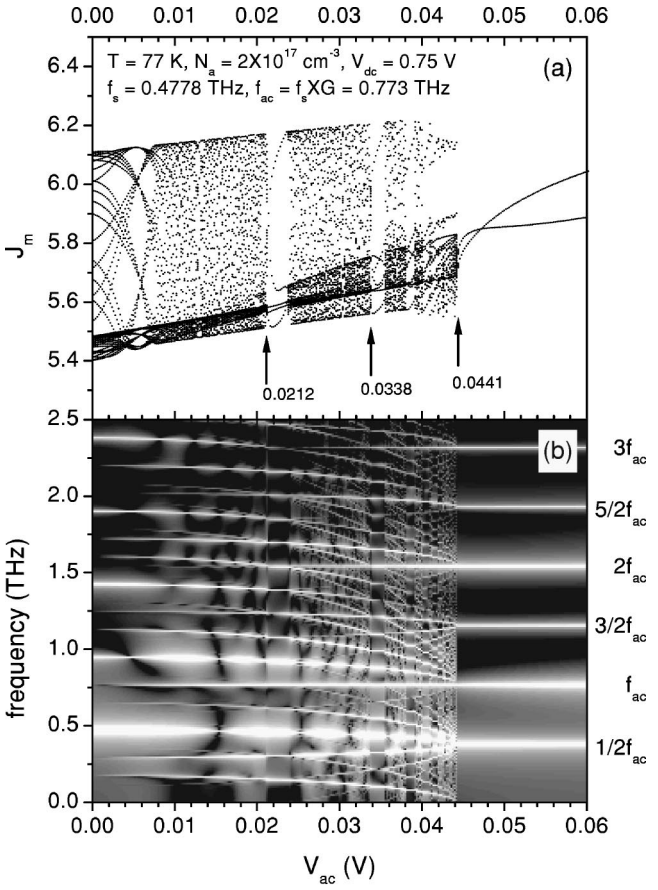

FIG. 10. (a) Poincaré bifurcation diagram and (b) power spectrum bifurcation diagram at $T=77$ K, $N_a=2\times10^{17}$ cm^{-3}, $V_{\rm dc}=0.75$ V, $f_s=0.4778$ THz, and $f_{\rm ac}=f_s\times G\approx0.773$ THz with G the inverse Golden mean ratio.

$\times10^{17}$ cm^{-3} at $T=77$ K. The ac frequency is fixed to the inverse golden mean G [$\equiv(1+\sqrt{5})/2=1.618\ldots$] times the self-oscillating frequency, i.e., $f_{\rm ac}=G\times f_0\approx1.36$ THz. The inverse golden mean ratio is often used in driving nonlinear systems[4,11,35] because it is regarded as the most irrational of all irrational numbers. To clarify the periodic and chaotic regions in controlling parameter space of $V_{\rm ac}$, we need the help of Poincaré bifurcation diagram. We define Poincaré mapping as follows. Let $T_{\rm ac}=1/f_{\rm ac}$ be the driving period. We use the current densities at times $t_m=mT_{\rm ac}$, $m=1,2,3,\ldots$, (after the transients die out) as the Poincaré mapping for each $V_{\rm ac}$. We compute $J_m=J(t_m)$ until the solution becomes periodic within a 10^{-4} accuracy, and depict all the J_m as the maps of $V_{\rm ac}$. If the solution J_m is aperiodic, we eliminate the first 30 transient points and depict the next 50 points of J_m. In the calculation, $V_{\rm ac}$ is changed from 0 to 0.09 V with a step of 0.2 mV. The calculated Poincaré bifurcation diagram is shown in Fig. 9(a), which indicates that there exist 2-, 5-, 7-, 9-, and 12-periodic windows and beyond all the periodic windows the spatiotemporal solutions become chaotic. Over the range of parameter $V_{\rm ac}$ from 0 to 0.09 V, we have not found any quasiperiodic solution (which can be verified by plotting first return map for each $V_{\rm ac}$, as discussed in the following). For small ac amplitude $V_{\rm ac}<0.0362$ V the system behaves chaotically. As $V_{\rm ac}$ increases, 5-periodic solutions (i.e., the frequency of the solution is 5 times ac driving frequency) span a wider window from $V_{\rm ac}=0.0362$ to 0.0436 V. With increasing $V_{\rm ac}$ 7-, 9-, and 12-periodic windows are observed, and the widths of the windows become narrower and narrower when the frequency of the solution increases. When $V_{\rm ac}>0.0628$ V the solutions become 2-periodic. In Fig. 9(b) we show the corresponding PS bifurcation diagram, where lighter areas correspond to larger amplitudes of PSs. The PS bifurcation diagram clearly displays the transitions between periodic and chaotic states. As $V_{\rm ac}$ approaches 0.0362 V, the chaotic behavior disappears abruptly and 5-periodic window appears with the frequency spectra consisting of $m/5$ ($m=1,2,3,\ldots$) times the driving frequency $f_{\rm ac}$. When $V_{\rm ac}$ reaches 0.0498 V, the solutions become 7-periodic with the frequency spectra consisting of $m/7$ ($m=1,2,3,\ldots$) times the driving frequency. Outside of these periodic windows, there seem to be a number of rather narrow chaotic windows. However, the transitions from the chaotic to the periodic windows occur over a very small voltage range and the frequency spectra become smeared out, thus not well resolved in Fig 9(b). The PS bifurcation diagram also clearly shows the coupling of dc bias and ac driving voltage. Near the left and right axes of Fig. 9(b), we have shown the positions of fundamental frequencies

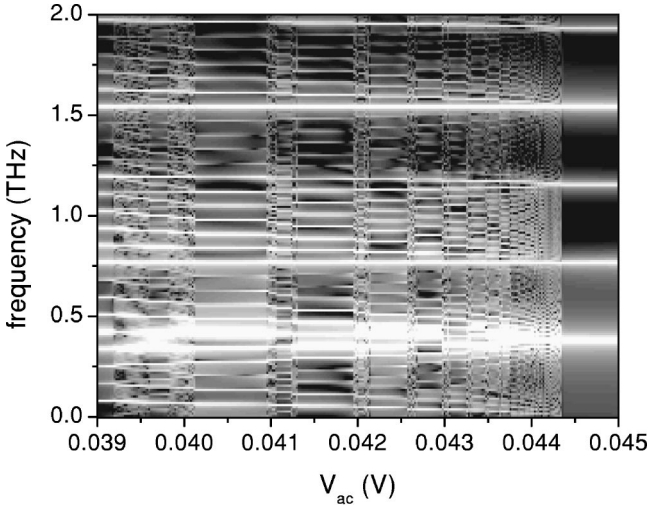

FIG. 11. Power spectrum bifurcation diagram for $V_{\rm ac}$ from 0.039 to 0.045 V. The parameters are the same as those described in Fig. 10.

f_s,$2f_s$,$3f_s$,$4f_s$, and the driving frequencies $mf_{\rm ac}/2(m=1,2,\ldots,6)$. When $V_{\rm ac}$ increases, the $f_{\rm ac}$ line becomes lighter and thinner, thus indicating ac voltage to play an increasing role on the behavior of carrier motion. In the meantime, the f_s line becomes darker and thicker with increasing ac voltage, and finally disappears when the system displays a 2-periodic solution at $V_{\rm ac}=0.0628$ V. The PS bifurcation diagram calculated here for the NEM diode is somewhat similar to that experimentally observed in doped superlattices.[4]

More complicated Poincaré and PS bifurcation diagrams are shown in Fig. 10 for another NEM p^+pp^+ diode having $N_a=2.0\times10^{17}$ cm^{-3} at $T=77$ K. The dc bias is set to be $V_{\rm dc}=0.75$ V, which leads to a self-oscillating frequency $f_s=0.4778$ THz. The driving frequency is fixed at $f_{\rm ac}=f_s\times G\approx0.773$ THz. It is shown in Fig. 10 that there are three main periodic windows: 5-periodic, 7-periodic, and 9-periodic. The oscillation alternates behavior between the periodic and chaotic states, resulting in a number of crossings of frequency peak lines. Each frequency branch splits into two or three branches. When the branches cross, they are locked to new periodic states. The periodic windows, however, are very narrow. This alternate transition becomes more and more frequent with increasing driving amplitude before the system finally enters the 2-periodic solution at $V_{\rm ac}>0.0441$ V. To have a clear insight into these transitions, we show in Fig. 11 the high-resolution PS bifurcation diagram for $V_{\rm ac}\in[0.039,0.045\ {\rm V}]$ calculated by setting the step of $V_{\rm ac}$ to be 0.02 mV. It is indicated that there are more complicated frequency bifurcations between the periodic and chaotic windows. These frequency cascades have resulted in the complicated mosaic structure, which exhibits a self-similarity of the pattern. In Fig. 12 we have shown the first return maps for six specific ac voltages in Fig. 10: (a) $V_{\rm ac}=0.01$, (b) 0.023, (c) 0.028, (d) 0.035, (e) 0.036, and (f) 0.043 V, respectively. The first return maps are obtained by plotting J_{m+1} as a function of J_m, where m is large enough such that the transient state dies out. First return map can

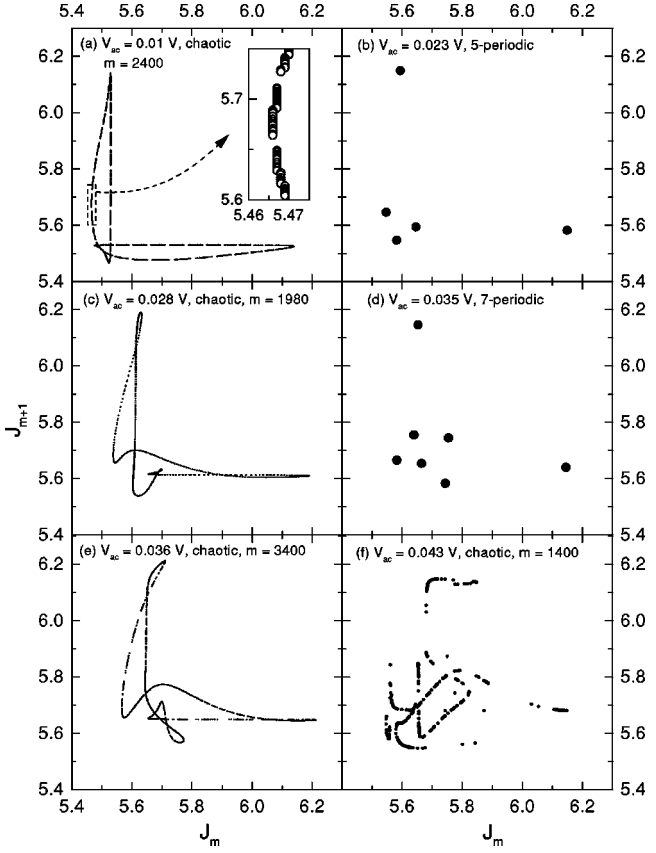

FIG. 12. First return maps at $V_{\rm ac}=0.01$, 0.023, 0.028, 0.035, 0.035, and 0.043 V, respectively, for the NEM p^+pp^+ diode described in Fig. 10.

often be used in distinguishing the quasiperiodic solution from chaotic solution. The resultant attractors for m-periodic solutions are just the m separate points [see Fig. 12(b) and (d)], while the chaotic attractors contain infinite random points (when $m\to\infty$) forming several separate branches [Fig. 12(f)] or a multilayered structure with varying density of the points on different regions [Fig. 12(a), (c), and (e)]. It is well known that the first return map of a quasiperiodic motion[11] is a closed smooth curve with regular distribution of the points. We have checked the first return maps for each $V_{\rm ac}$ and have not found any closed smooth curve, thus confirming that no quasiperiodic solution exists in the full region of parameter $V_{\rm ac}$ considered here.

Finally, we have studied the response of the NEM p^+pp^+ diode system under different driving frequency $f_{\rm ac}$ when fixing $V_{\rm dc}$ and $V_{\rm ac}$. In Fig. 13, we show Poincaré and PS bifurcation diagrams at $T=77$ K, $N_a=2.0\times10^{17}$ cm^{-3}, $V_{\rm ac}=0.036$ V, and $V_{\rm dc}=0.75$ V. The self-oscillating frequency is $f_s=0.4778$ THz. We change the driving frequency from $f_{\rm ac}/f_s=0$ to 5.6. It is shown that there are five main periodic windows indicated in Fig. 13(a) by *A*: 1-periodic, *B*: 2-periodic, *C*: 3-periodic, *D*: 4-periodic, and *E*: 5-periodic. These m-periodic ($m=1,2,\ldots,5$) windows lie in the driving frequency bands near $f_{\rm ac}/f_s=m$. All the frequency bifurcations in the periodic windows shown in Fig. 13(b) are linear combinations of the driving frequency $f_{\rm ac}$. However, those in the chaotic windows are complicated, which are the com-

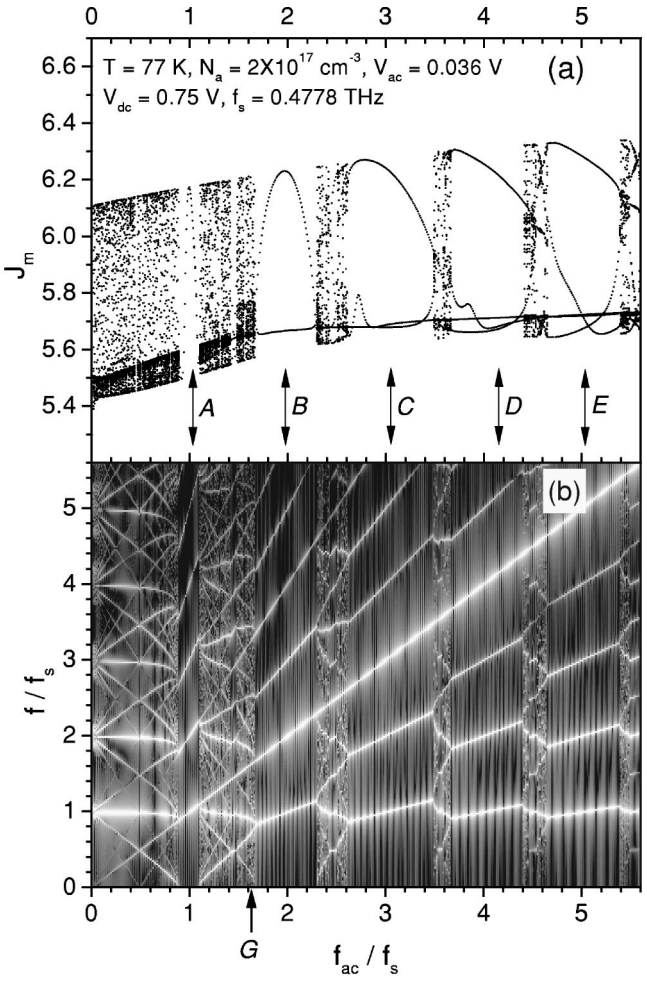

FIG. 13. (a) Poincaré bifurcation diagram and (b) power spectrum bifurcation diagram by changing $f_{ac}/f_s=0$ to 5.6 at $T=77$ K, $N_a=2.0\times10^{17}$ cm^{-3}, $V_{ac}=0.036$ V, $V_{dc}=0.75$ V, and $f_s=0.4778$ THz.

binations of two independent frequencies f_s and f_{ac}. Actually, the chaotic state attains a higher complexity near the frequency $f_{ac}/f_s=G$. The scenario of chaotic and periodic behavior is associated with a characteristic self-similar emergence of high-order mixing frequencies. We expect that there are some sets of parameters which can produce much more complicated PS bifurcation diagrams for the NEM p^+pp^+ diode. In Fig. 14, we have studied in detail four specific cases of Fig. 13 with the driving frequencies: (a) $f_{ac}=0.5$, (b) 1.0, (c) 2.4, and (d) 2.67 THz, respectively. We have plotted in Fig. 14 the time-dependent currents $J(t)$ (left), power spectra $P(f)$ (middle, arbitrary unit), and phase portraits (right). The phase portrait is often used in detecting the chaotic characteristics of a time series. The phase portraits $J(t)$ vs $V(t)$ shown in the right of Fig. 14 could be measured experimentally by depicting the current in the external circuit as a function of the instantaneous applied voltage $V(t)$. Cases (a), (b), and (c) correspond 1-, 2-, and 5-periodic solutions, respectively, and case (d) is in chaotic state. It can be seen that the PSs for the m-periodic solutions [Figs. 14(a), (b), and (c)] are relatively smooth and just have m peaks in the frequency band of $f/f_{ac}\in(i-1,i]$ $(i=1,2,3,\ldots)$, corresponding the driving frequency f_{ac} and its harmonics. However, for the chaotic solution [Fig. 14(d)] the PSs become very irregular with a large number of peaks. The phase portraits for the periodic solutions appear as simple closed loops [Figs. 14(a)–14(c)], while the one for the chaotic solution becomes very much folder and irregular [Fig. 14(d)].

V. CONCLUSIONS AND REMARKS

We have theoretically investigated the nonlinear dynamic characteristics of NEM p^+pp^+ diodes driven by dc and ac voltages in the form of $V(t)=V_{dc}+V_{ac}\sin(2\pi f_{ac}t)$, based on the nonparabolic balance-equation theory and the transient drift-diffusion model. Depending on the model NEM dispersion given by Eq. (1), we obtain an ''N-shaped'' velocity-field relation, i.e., after the NDV disappears there is a positive-differential-velocity region. When the NEM p^+pp^+ diode is subjected to a dc bias in the NDV region, the dynamic electric field domain is formed, leading to a current self-oscillation with a frequency in the THz range. The self-oscillating frequency and time-averaged current are extensively studied for the p^+pp^+ diodes at different doping concentration and lattice temperature. In contrast, when the NEM p^+pp^+ diodes are driven both by dc and ac voltages, various types of spatiotemporal behaviors and current-voltage characteristics are found with changing the controlling parameters V_{dc}, V_{ac}, and f_{ac}. The Poincaré and power spectrum bifurcation diagrams are calculated in order to clarify the transition between the periodic and chaotic windows in the controlling parameter space. When the driving frequency is fixed to the fundamental frequency times the inverse Golden mean ration, the power spectrum bifurcation diagram has a complex mosaic pattern with a self-similar emergence of high-order mixing frequencies. We expect that there are some sets of parameters which may produce much more complicated bifurcation scenarios. The present study may be useful in utilizing and in controlling the possible chaos in p-QW-based modern devices, such as quantum-well infrared photo-detector[36–42] and parallel asynchronous multispectral focal-plane sensor.[43]

The present investigation focuses on the complex and interesting nonlinear dynamics in semiconductors with an NEM dispersion. It is the first time, to our knowledge, that the theoretical calculations address the power spectrum bifurcation diagrams [see Fig. 10(b)] having such a complicated mosaic structure with a self-similar emergence of high-order mixing frequencies. In principle, it is no problem for us to carry out a study by directly solving hydrodynamic balance equations (HBE's), as we analyzed spatiotemporal domain and chaos in miniband superlattices.[18] For the sake of simplicity in the present calculations we have used the DD model rather than the HBE. The basic considerations are as follows.

(1) This article addresses a model calculation of field-domain-related carrier transport and nonlinear dynamics in semiconductors having a NEM dispersion. The main purpose is to investigate the nonlinear characteristics of a THz-driven p^+pp^+ diode if the p-base carrier has a NEM. We assume

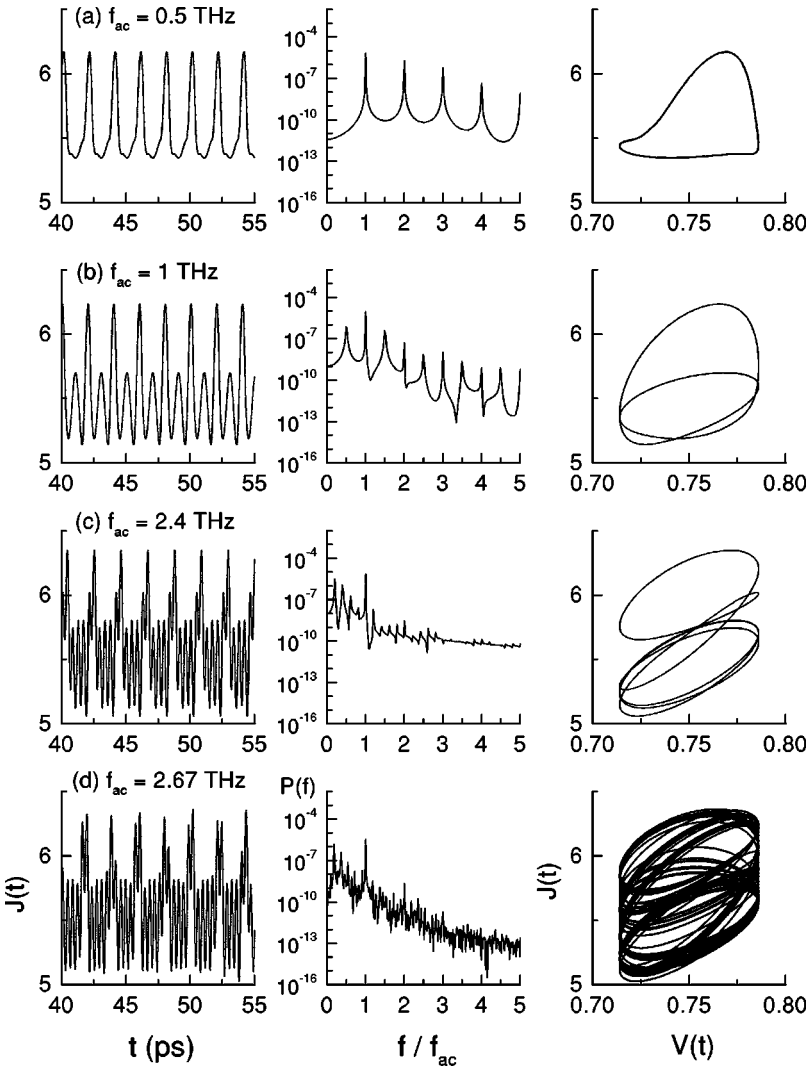

FIG. 14. Time-dependent current densities $J(t)$ (left), power spectra $P(f)$ (middle, arbitrary unit), and phase portraits (right) at four specific ac frequencies $f_{ac}=0.5$, 1, 2.4, and 2.67 THz for the NEM p^+pp^+ diode described in Fig. 13.

that the NEM dispersion is given by the outside procedure either by an experiment[23] or by an energy-band calculation.[24] The dispersion with a NEM section assumed by Eq. (1) may be abstracted from the hole subband dispersion of *p*-type QW.[24] So, according to the present calculations, it may be possible to design oscillators having different self-oscillating frequency and mixing mode of current oscillation by changing the QW parameters. It is noted that two designs of the ballistic terahertz (THz) generators based on the NEM hole dispersion have recently been suggested.[29]

(2) The ''*N*-shaped'' velocity-field relation is obtained by using the three-dimensional nonparabolic balance-equation theory with a realistic treatment of carrier scatterings by impurity, acoustic phonon, and optic phonons. Band nonparabolicity and quantum-mechanical effects are included in the balance-equation formulas. The resulting velocity-field relation (or mobility) is input into the DD model to investigate the nonlinear dynamical characteristics of a semiconductor with NEM dispersion. The microscopic information about energy dispersion and scattering process therefore enters into the calculation of the macroscopic DD model by the mobility and diffusion coefficient. In fact, the power spectrum scenarios calculated here are very similar to those from experiments for sequential resonant tunneling superlattice,[4,44] whose velocity-field relation behaves ''*N*-shaped.'' In principle, the case of two-dimensional (2D) quantized carriers confined in QW's can be considered in a similar manner by the well-established 2D balance-equation theory.[17,46]

(3) The DD model has been successfully used to investigate current instabilities in Gunn-effect-like devices over the past several decades. Recently, the discrete DD model once more showed its validity in studying nonlinear dynamical characteristics of sequential resonant tunneling superlattices[10–12] and field-domain-related problems induced by a transverse magnetic field in a doped GaAs/AlAs superlattice.[45] From the viewpoint of physics, the formation of field domain is the direct result of inhomogeneous traveling charge density waves. The DD model accounts for the spatial inhomogeneity by the carrier density diffusion term.

(4) One of the feasible realizations of the present theoretical prediction is THz oscillators based on GaAs/AlAs *p*-QW, in which quantized holes are the dominant carriers. The use of the DD model is partially supported by the fact that hole temperature usually remains close to lattice temperature in contrast to electron temperature, which is hot at high electric fields. It is believable that the hot-carrier effect

does not play a main role on carrier transport in the present model calculations. On the other hand, we note that, for the electrons in superlattices, the electron temperature is not very hot in most cases [$T_e/T<2$, see Fig. 3(b) in Ref.18].

(5) To yield a reasonable accuracy of the calculations, we must use more spatial meshpoints and shorter temporal intervals in discretizing the equations. Here, we apply 300 spatial meshpoints and 1.5×10^{-3} ps time step. The time delay that we have calculated is usually greater than $120T_{ac}$ for accurately calculating the power spectrum of current density by using a fast Fourier transform algorithm. In order to save computing time and to do more extensive examinations by varying device parameters, we therefore select the DD model for the present computation intensive calculations. The HBE's are much more sophisticated and time consuming than the DD model. As further work, we may use HBE's to study the same problem and find the differences and connections between the two models.

ACKNOWLEDGMENTS

This work was partially supported by the Special Funds for Major State Basic Research Project No. G20000683, the National Natural Science Foundation of China, the Ministry of Science and Technology of China, and the Shanghai Foundation for Research and Development of Applied Materials.

*Electronic mail: jccao@mail.sim.ac.cn

[1] B. J. Keay, S. J. Allen, Jr., J. Galán, J. P. Kaminski, K. L. Campman, A. C. Gossard, U. Bhattacharya, and M. J. W. Rodwell, Phys. Rev. Lett. **75**, 4098 (1995).

[2] B. J. Keay, S. Zeuner, S. J. Allen, Jr., K. D. Maranowski, A. C. Gossard, U. Bhattacharya, and M. J. W. Rodwell, Phys. Rev. Lett. **75**, 4102 (1995).

[3] K. Unterrainer, B. J. Keay, M. C. Wanke, S. J. Allen, D. Leonard, G. Medeiros-Ribeiro, U. Bhattacharya, and M. J. W. Rodwell, Phys. Rev. Lett. **76**, 2973 (1996).

[4] Y. H. Zhang, J. Kastrup, R. Klann, K. H. Ploog, and H. T. Grahn, Phys. Rev. Lett. **77**, 3001 (1996); Y. H. Zhang, R. Klann, H. T. Grahn, and K. H. Ploog, Superlattices Microstruct. **21** (4), 565 (1997).

[5] K. J. Luo, H. T. Grahn, K. H. Ploog, and L. L. Bonilla, Phys. Rev. Lett. **81**, 1290 (1998); K. J. Luo, H. T. Grahn, and K. H. Ploog, Phys. Rev. B **57**, R6838 (1998).

[6] E. Schomburg, A. A. Ignatov, J. Grenzer, K. F. Renk, D. G. Pavel'ev, Yu. Koschurinov, B. Ya. Melzer, S. Ivanov, S. Schaposchnikov, and P. S. Kop'ev, Appl. Phys. Lett. **68**, 1096 (1996).

[7] E. Schomburg, T. Blomeier, K. Hofbeck, J. Grenzer, S. Brandl, I. Lingott, A. A. Ignatov, K. F. Renk, D. G. Pavel'ev, Yu. Koschurinov, B. Ya. Melzer, V. M. Ustinov, S. V. Ivanov, A. Zhukov, and P. S. Kop'ev, Phys. Rev. B **58**, 4035 (1998).

[8] N. G. Asmar, A. G. Markelz, E. G. Gwinn, J. Čeme, M. S. Sherwin, K. L. Campman, P. F. Hopkins, and A. C. Gossard, Phys. Rev. B **51**, 18 041 (1995).

[9] N. G. Asmar, J. Čeme, A. G. Markelz, E. G. Gwinn, M. S. Sherwin, K. L. Campman, and A. C. Gossard, Appl. Phys. Lett. **68**, 829 (1996).

[10] O. M. Bulashenko and L. L. Bonilla, Phys. Rev. B **52**, 7849 (1995).

[11] O. M. Bulashenko, M. J. García, and L. L. Bonilla, Phys. Rev. B **53**, 10 008 (1996).

[12] O. M. Bulashenko, K. J. Luo, H. T. Grahn, K. H. Ploog, and L. L. Bonilla, Phys. Rev. B **60**, 5694 (1999).

[13] K. N. Alekseev, G. P. Berman, D. K. Campbell, E. H. Cannon, and M. C. Cargo, Phys. Rev. B **54**, 10 625 (1996).

[14] K. N. Alekseev, E. H. Cannon, J. C. McKinney, F. V. Kusmartsev, and D. K. Campbell, Phys. Rev. Lett. **80**, 2669 (1998).

[15] A. A. Ignatov and A. P. Jauho, J. Appl. Phys. **85**, 3643 (1999).

[16] X. L. Lei, J. Appl. Phys. **82**, 718 (1997).

[17] X. L. Lei, B. Dong, and Y. Q. Chen, Phys. Rev. B **56**, 12 120 (1997).

[18] J. C. Cao and X. L. Lei, Phys. Rev. B **59**, 2199 (1999).

[19] J. C. Cao and X. L. Lei, Phys. Rev. B **60**, 1871 (1999).

[20] J. C. Cao, H. C. Liu, and X. L. Lei, Phys. Rev. B **61**, 5546 (2000).

[21] J. C. Cao, H. C. Liu, and X. L. Lei, J. Appl. Phys. **87**, 2867 (2000).

[22] K. Unterrainer, in *Intersubband Transitions in Quantum Wells: Physics and Device Applications II*, edited by H. C. Liu and F. Capasso (Academic Press, San Diego, 2000), Chap. 3, p. 127.

[23] R. K. Hayden, D. K. Maude, L. Eaves, E. C. Valadares, M. Henini, F. W. Shears, O. H. Hughes, J. C. Portal, and L. Cury, Phys. Rev. Lett. **66**, 1749 (1991).

[24] J. A. Kash, M. Zachau, M. A. Tischler, and U. Ekenberg, Semicond. Sci. Technol. **9**, 681 (1994).

[25] N. Z. Vagidov, Z. G. Gribnikov, and A. N. Korshak, Semiconductors **29**, 1014 (1995).

[26] Z. S. Gribnikov, A. N. Korshak, and N. Z. Vagidov, J. Appl. Phys. **80**, 5799 (1996).

[27] A. N. Korshak, Z. S. Gribnikov, N. Z. Vagridov, S. I. Kozlovsky, and V. V. Mitin, Phys. Status Solidi B **204**, 80 (1997).

[28] Z. S. Gribnikov, A. N. Korshak, and V. V. Mitin, Int. J. Infrared Millim. Waves **20**, 213 (1999).

[29] A. N. Korshak, Z. S. Gribnikov, N. Z. Vagidov, and V. V. Mitin, Appl. Phys. Lett. **75**, 2292 (1999).

[30] Z. S. Gribnikov, N. Z. Vagidov, A. N. Korshak, and V. V. Mitin, J. Appl. Phys. **87**, 7466 (2000).

[31] X. L. Lei, J. Cai, and L. M. Xie, Phys. Rev. B **38**, 1529 (1988); X. L. Lei, Phys. Status Solidi B **192**, K1 (1995).

[32] X. L. Lei, N. J. M. Horing, and H. L. Cui, Phys. Rev. Lett. **66**, 3277 (1991); J. Phys.: Condens. Matter **4**, 9375 (1992).

[33] X. L. Lei, J. C. Cao, and B. Dong, J. Appl. Phys. **80**, 1504 (1996).

[34] J. B. Gunn, Solid State Commun. **1**, 88 (1963).

[35] E. Ott, *Chaos in Dynamical Systems* (Cambridge University Press, Cambridge, 1993).

[36] H. C. Liu, J. Li, M. Buchanan, and Z. R. Wasilewski, IEEE J. Quantum Electron. **32**, 1024 (1996).

[37] H. C. Liu, L. Li, M. Buchanan, Z. R. Wasilewski, G. J. Brown, F. Szmulowicz, and S. M. Hegde, J. Appl. Phys. **83**, 585 (1998).

[38] H. C. Liu, F. Szmulowicz, Z. R. Wasilewski, M. Buchanan, and G. J. Brown, J. Appl. Phys. **85**, 2972 (1999).

[39] H. C. Liu, in *Intersubband Transitions in Quantum Wells: Physics and Device Applications I*, edited by H. C. Liu and F. Ca-

passo (Academic Press, San Diego, 2000), Chap. 3, p. 129.
[40] A. G. U. Perera and S. G. Matsik, Appl. Phys. Lett. **67**, 962 (1995).
[41] A. G. U. Perera, W. Z. Shen, S. G. Matsik, H. C. Liu, M. Buchanan, and W. J. Schaff, Appl. Phys. Lett. **72**, 1596 (1998).
[42] A. G. U. Perera, V. G. Silvestrov, S. G. Matsik, H. C. Liu, M. Buchanan, Z. R. Wasilewski, and M. Ershov, J. Appl. Phys. **83**, 991 (1998).
[43] A. G. U. Perera, in *Homojunction and Quantum-Well Infrared Detectors*, edited by M. H. Francombe and J. L. Vossen (Academic Press, San Diego, 1995), p. 1.
[44] N. Ohtani, N. Egami, K. Fujiwara, and T. Grahn, Solid-State Electron. **42**, 1509 (1998).
[45] B. Sun, J. Wang, W. Ge, Y. Wang, D. Jiang, H. Zhu, H. Wang, Y. Deng, and S. Feng, Phys. Rev. B **60**, 8866 (1999).
[46] X. L. Lei, J. L. Birman, and C. S. Ting, J. Appl. Phys. **58**, 2270 (1985); H. L. Cui, X. L. Lei, and N. J. M. Horing, Phys. Rev. B **37**, 8223 (1988).